minerals

MDPI

Article

Multi-Technique Characterization of a Fine Fraction of CDW and Assessment of Reactivity in a CDW/Lime System

Moisés Frías [1], Raquel Vigil de la Villa [2], Sagrario Martínez-Ramírez [3], Lucía Fernández-Carrasco [4], Ernesto Villar-Cociña [5] and Rosario García-Giménez [2,*]

[1] Eduardo Torroja Institute for Construction Science (IETcc-CSIC), 28033 Madrid, Spain; mfrias@ietcc.csic.es
[2] Departamento de Geología y Geoquímica, Geomateriales Unidad Asociada CSIC-UAM, Universidad Autónoma de Madrid, 28049 Madrid, Spain; raquel.vigil@uam.es
[3] Institute for the Structure of Matter (IEM-CSIC), 28006 Madrid, Spain; sagrario@iem.cfmac.csic.es
[4] Department of Civil and Environmental Engineering, Barcelona TECH, Universitat Politècnica de Catalunya, 08034 Barcelona, Spain; lucia.fernandez@upc.edu
[5] Department of Physics, Central University of Las Villas, Santa Clara 54830, Villa Clara, Cuba; evillar@uclv.edu.cu
* Correspondence: rosario.garcia@uam.es

Received: 3 June 2020; Accepted: 29 June 2020; Published: 30 June 2020

Abstract: This study analysed the fine particle (<5 mm) waste generated during siliceous or calcareous (depending on the composition of the original aggregate) concrete waste crushing. In the absence of industrial applications, such waste is amassed in open-air stockpiles on construction and demolition wastes (CDW) management plant grounds. The aim pursued was to find an outlet for that material in the cement industry. The starting waste, sourced from six Spanish management facilities, was characterised for its chemical and mineralogical composition, physical properties and pozzolanicity. The mineralogical phases in the CDW/lime system and their variations during the pozzolanic reaction were likewise identified. The findings showed that the fine waste consisted primarily in quartz, calcite, micas and feldspars, with smaller fractions of kaolinite and cement anhydrous phases. No portland cement hydration phases were identified. All six types analysed exhibited medium to low pozzolanicity, with the highest values recorded for the siliceous waste. Ettringite, C–S–H gels and calcium aluminate hydrates (C_4AH_{13}, C_4AcH_{12}) were identified during the pozzolanic reaction in CDW/lime system. Therefore, this type of waste can be reused as supplementary cementitious material with low-medium pozzolanic activity.

Keywords: fine particle waste; concrete-based CDW; mineralogy; pozzolanicity; hydrated phases

1. Introduction

Although the construction industry is one of the mainstays of countries socio-economic development, it is directly associated with adverse environmental impacts such as high energy consumption and global warming, among others [1]. In addition, the large volumes of non-biodegradable construction and demolition wastes (CDW) generated at the end of a structure's service life are normally stockpiled in landfills, prompting economic, technical, environmental and social problems [2,3].

The 820 Mt/year of CDW generated in Europe account for 50% of the continental total [4]. An estimated 43% of such CDW is landfilled [5]. In the wake of the 2009 economic crisis and its severe implications for Spain, only 10% of the nation's mean 1.31 Mt/year or 0.28 t/inhabitant/year of waste generated between 2011 and 2015 was recycled [6].

Sustainable development and circular economy policies presently prioritise the valorisation of industry waste and rubble as secondary raw materials [7,8]. Construction and demolition waste must be handled at specialised management plants for subsequent use. The inorganic fraction remaining after removal of wood, plastic, metals, textiles, electronic devices and so on consists primarily in concrete and mixed (clay-based and cement matrix) materials, generally used in road bases, sub-bases, subgrades, landfills and as graded aggregate, among others [9–13].

In recent years, however, in light of the high cementitious material content in this inorganic waste, research has turned its focus to reuse in construction materials [14] for liquid radioactive waste containment [15], as pozzolans [16–19] or in clinker [20] or brick [21] manufacture. Much worldwide research conducted on the use of such waste in eco-efficient mortars and concretes has shown its technical, economic and environmental viability as recycled aggregate. Concrete-based aggregate has attracted particular attention [22–25] and its use is now envisaged in international standards, regulations instructions and reports [4,26,27]. At the European level, countries such as Spain [28] Belgium [29], Germany [30], Italy [31], the United Kingdom [32], allow a percentage of replacement of concrete crushing aggregate between 15%–60% of the coarse fraction for the manufacture of structural concrete.

Not all this waste is recycled, however, for the crushing entailed to produce aggregate of suitable particle size generates fine, <5 mm particle materials, comprising primarily fine aggregates, hydrated cement paste and impurities. In the absence of any industrial use, these materials are stockpiled on management plant grounds [33]. Currently, there is a large scientific gap related to this topic, so no previous references have been found that address this type of waste accumulated outdoors, so the need arises to seek a viable reuse as an alternative to its stockpiling.

This study consequently undertook a first-time analysis of the scientific viability of applying six types of fine-particle concrete waste varying in nature and sourced from different management plant stockpiles as future eco-efficient pozzolans. The starting materials and their pozzolanicity were fully characterised and the variations in their mineralogical phases during reactions in the pozzolan/lime system were identified. The ultimate aim was to establish the scientific grounds for understanding the physical–mechanical behaviour of the respective blended cement matrices.

2. Materials and Methods

2.1. Materials

Six types of discarded fine (<5 mm) particle waste resulting from crushing concrete-based CDW at six specialised management plants were selected for this study.

Three materials based on concrete originally manufactured with siliceous aggregate (HsT, HsC and HsS) were supplied by plants in central Spain (Greater Madrid and Castile-La Mancha) and the other three on concrete bearing calcareous aggregate (HcG, HcV and HcL) furnished by plants in northern Spain (Basque Country).

Upon receipt at the laboratory the fines were oven dried at 105 °C for 24 h and subsequently ground in a ball grinder to a particle size of under 63 μm, the optimal size for use as an active cement addition (Figure 1). Some agglomerations of the finest particles during storage are observed in the figure, which are easily dispersed when introduced into the saturated lime solution.

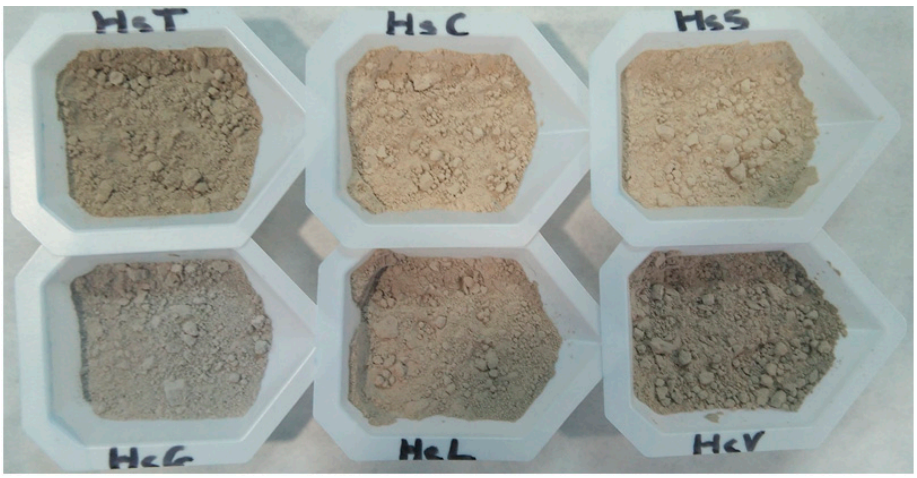

Figure 1. Samples after grinding and sieving to <63 μm.

2.2. Methods

2.2.1. Pozzolanicity Test

Waste pozzolanicity was assessed with an accelerated method in a pure pozzolan/calcium hydroxide (lime) system. In this chemical procedure, 1g of waste was added to 75 mL of a saturated (17.68 mmol/L) lime solution prepared with extra pure (Ph. Eur., USP, BP) calcium hydroxide and stored at 40 °C in a laboratory oven for 1 day, 7 days, 28 days and 90 days. At the specified time, the solutions were filtered and titrated with EDTA to determine their lime content. The amount of lime fixed was determined as the difference between the lime present in a reference solution and the amount in the test solutions at each age. The solid residues, in turn, were rinsed with ethanol and dried in an electric oven at 60 °C for 24 h to detain the pozzolanic reaction.

2.2.2. Instrumental Techniques

The chemical and mineralogical composition of the starting materials and hydrated phases were as characterised with the instrumental techniques described below.

The main oxides were identified by X-ray fluorescence on a Philips PW-1404 spectrometer (Philips, Madrid, Spain) fitted with a Sc-Mo X-ray tube.

CDW fineness and particle size distribution were analysed with dry dispersion mode laser diffraction on a Malvern Mastersizer 3000 analyser (Aero S; Malvern Pananalytical, Madrid, Spain) fitted with red and blue (He-Ne and LED) light sources and featuring a measuring range of 0.01 μm to 3500 μm.

Whole sample mineralogy was determined with powder X-ray diffraction (XRD) on a PAN Analytical X'Pert Pro X-ray diffractometer (Pananalytical, Davis, CA, USA) fitted with a Cu anode. The operating conditions were 40 mA, 45 kV, divergence slit of 0.5° and 0.5 mm reception slits. The powder samples were scanned with a step size of 0.0167 (2θ) at 150 ms per step and 2θ angles of 5° to 60° [34] using rutile as an internal standard. Rietveld quantification was conducted with Match v.3 and Fullprof suite software [35–38]. The phases detected were identified using the Crystallography Open Database (COD) collection of crystal structures.

SEM/EDX morphological studies and sample surface quantification were performed on an FEI Company Inspect (W source) scanning electron microscope (Hillsboro, OR, USA), fitted with an energy dispersive X-ray DX4i analyser and Si/Li detector. The chemical composition shown is the mean of 10 readings per point analysed.

MAS NMR analyses were run on a Bruker Avance-400 spectrometer (Bruker, Kontich, Belgium) under the following conditions: ^{29}Si resonance frequency, 79.5 MHz; spinning rate, 10 kHz; pulse sequence, single 5 μs pulse with a recycle delay of 10 s; number of transients, 8192; and external standard, tetramethylsilane (TMS); ^{27}Al resonance frequency, 104.3 MHz; spinning rate, 10

kHz; pulse sequence, single 2 μs pulse with a recycle delay of 5 s; number of transients, 400; and external standard, $Al(H_2O)_6^{3+}$.

The dry, homogenised powder samples of both the starting materials and the lime-soaked samples were characterised in the mid-infrared range with Fourier transform infrared spectroscopy on a Bruker Alpha FTIR spectrometer (Bruker, Barcelona, Spain) featuring a spectral range of 375 cm^{-1} to 7500 cm^{-1}, a standard 500 cm^{-1} to 7500 cm^{-1} KBr beam splitter and spectral resolution of 2 cm^{-1}. KBr wafers were prepared to study the samples under infrared light by pressing 1.7 mg of sample into 300 mg of KBr.

3. Results and Discussion

3.1. Starting Material Characterisation

The X-Ray Fluorescence (XRF) chemical findings for the concrete-based CDWs analysed are in Table 1. The oxide content distribution changed depending on the type of aggregate, with the greatest differences observed in SiO_2, CaO and Al_2O_3. Loss on ignition was also found to vary substantially.

In the waste bearing siliceous aggregate (HsT, HsC and HsS), SiO_2 accounted for 49.0% to 58.0% of the total, CaO for 14.5% to 21.4% and Al_2O_3 for 8.0% to 9.6%. In contrast, in the calcareous waste (HcG, HcL and HcV), SiO_2 ranged from 9.0% to 23.3%, CaO from 38.7% to 50.3% and Al_2O_3 from 2.9% to 6.6%. The findings for the siliceous concrete waste were consistent with results observed by Ulsen et al. [25] for crushed and ground (<3 mm) recycled siliceous wastes.

The K_2O content in the fine particle siliceous concrete waste (Hs), at 2.6% to 3.8%, in turn, was greater than the 0.5% to 2.2% found in the calcareous materials (Hc). Waste HsT had an SO_3 content of 2.5%, much higher than the 0.6% to 0.9% in the other materials analysed. The chloride content was under 0.03% in all the samples and loss on ignition (LOI) varied according on the aggregate nature: 8.7 wt% to 12.9 wt% for the siliceous and 25.7 wt% to 33.2 wt% for the calcareous waste. Waste HsC, with the highest calcite content of the three siliceous materials, also exhibited the greatest loss on ignition.

Table 1. X-Ray Fluoresecence (XRF)-determined chemical composition of fine particle construction and demolition wastes (CDW) waste (OPC = ordinary Portland cemnt; LOI = loss on ignition).).

	OPC	HsT	HsC	HsS	HcG	HcL	HcV
SiO_2	14.22	49.97	49.22	58.00	9.34	23.27	12.10
Al_2O_3	2.89	8.98	8.01	9.56	2.88	6.58	3.78
CaO	69.81	18.65	21.38	14.48	50.32	38.66	45.93
Fe_2O_3	3.70	2.30	2.19	2.12	1.20	2.30	2.49
MgO	0.93	1.37	1.58	1.11	1.12	0.78	0.92
SO_3	3.36	2.53	0.88	0.72	0.85	0.59	0.67
Na_2O	0.33	0.80	0.63	0.90	0.18	0.41	0.25
K_2O	0.76	3.35	2.61	3.83	0.47	1.07	0.72
P_2O_5	0.14	0.11	0.12	0.10	0.03	0.08	0.09
TiO_2	0.20	0.28	0.30	0.30	0.14	0.39	0.42
MnO	0.10	0.04	0.03	0.03	0.09	0.05	0.06
LOI	3.22	11.50	12.90	8.69	33.20	25.70	32.40

The particle size distribution (Figure 2) was bimodal in all the materials after grinding to <63 μm, although the variation in peak intensity from 6–8 μm to 33–35 μm attested to the differences in the majority mineral (calcite or quartz) hardness.

The similarity of fineness in the two types of samples was corroborated by their D_{10} (maximum mesh size passed by 10% of the sample) and D_{50} (by 50%) values: D_{10} = 1.00–1.10 μm and D_{50} = 8.00–9.30 μm in the siliceous waste (Hs); D_{10} = 0.80 μm to 0.86 μm and D_{50} = 5.20 μm to 5.80 μm in the calcareous CDW. On the grounds of those data, fineness would have practically no effect on the rate of the pozzolanic reaction.

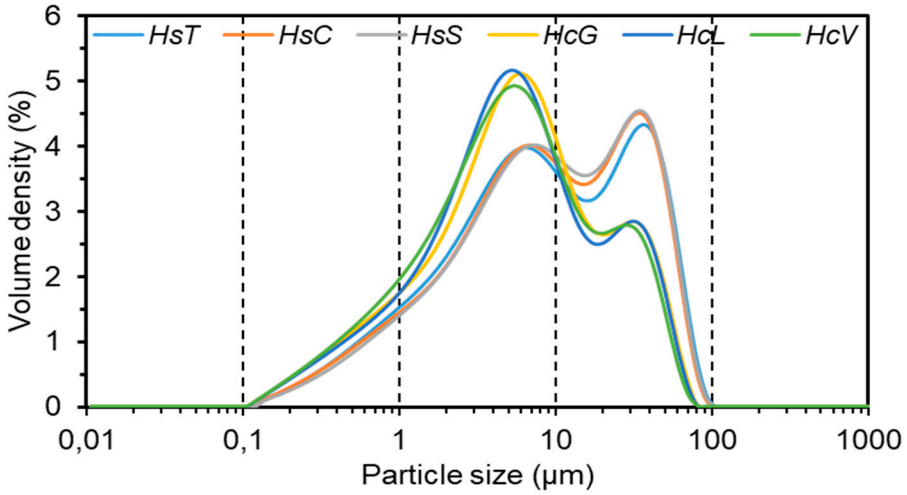

Figure 2. Laser diffraction-determined particle size distribution in fine particle CDW.

Further to the XRD mineralogical analysis, the composition was qualitatively similar in all the fine concrete-based waste, with phases such as calcite, mica, quartz and feldspars clearly present. Rietveld refinement (Table 2) identified differences in the percentage of these constituents depending on the aggregate nature in the recycled concrete. ICDD PDF-4+ numbers are mica (01-074-3152), quartz (00-033-1161), feldspar (00-013-0931), calcite (01-072-1937) and kaolinite (04-013-3074). Kaolinite was detected in concrete HcL only.

The primary source of the mineral phases observed was the aggregates used to manufacture the original concretes, although contamination by materials in the surrounds during management plant stockpiling cannot be ruled out. The calcite abundance in all the siliceous and calcareous waste may also be partially attributed to cement hydrated phase carbonation both during its service life and during storage on management plant grounds, given the particle size involved (<5 mm).

Table 2. Rietveld refinement of starting concrete waste.

Waste	Mica (%)	Quartz (%)	Feldspar (%)	Calcite (%)	Kaolinite (%)	Amorphous Material (%)	R_B	X^2
HsT	4	48	8	24	n.d.	16	17.6	7.3
HsC	6	49	6	28	n.d.	11	19.1	7.7
HsS	4	58	10	16	n.d.	12	22.3	8.2
HcG	10	10	11	52	n.d.	17	23.9	6.9
HcL	12	14	13	40	10	11	17.9	6.2
HcV	7	12	10	62	traces	9	16.8	5.7

n.d. = not detected; X^2: Rietveld goodness of fit; R_B: Bragg R factor.

As this fine particle waste was exposed to the elements under extreme weather conditions, XRD detected none of the hydrated cement phases (tobermorite, calcium aluminate, carboaluminate hydrate) that would initially be expected in post-service life concretes. That may be attributed to the small size of hydrated cement particles, which may have accelerated cement-based waste weathering and concomitant carbonated phase formation during exposure. In an earlier study using various characterisation techniques, Gebauer and Harnit [39] identified C–S–H gels; CH and carboaluminate hydrate in a cement sample paste drawn from concrete in an 84-year-old bridge. Those findings could not be compared to the present data or extrapolated, however, inasmuch as the authors did not specify the exact position or orientation of the host concrete.

The amorphous material in turn, comprising 9% to 17% of the total in the present samples, may have included C–S–H gel. Moreover, as the concentration of hydrated crystalline phases may have been below the XRD detection limit, SEM, ^{27}Al NMR, ^{29}Si NMR and FTIR analyses were conducted to identify any possibly present. ^{27}Al NMR and ^{29}Si NMR analyses indicated only the presence of the compounds with Al and Si respectively, then it is a very good option to determine

C–S–H and aluminates compounds in low concentration. From ^{29}Si NMR only compounds with Si are detected, and then the proportion of those compounds will be under XRD detection. It is possible that some compound will be detected by NMR and not by XRD. The compounds not crystalline (type gels) show these signal [40].

According to the SEM/EDX morphological findings, all the waste present grains whose composition matched that of the minerals detected with XRD. Their particle sizes ranged mostly from 10 μm to 20 μm, values consistent with the laser diffraction results. In all six types of waste the surfaces were highly flawed with defects such as voids and fractures and randomly distributed deposits (described as amorphous phases) comprising variable amounts of elements such as magnesium, sulphur, iron, potassium and calcium (Figures 3 and 4; Tables 3 and 4).

A detailed analysis of the smallest aggregates in the waste denoted differences in their compactation degree. The calcareous waste was observed to contain twisted aggregates consisting in small fragments clustering around distribution cores (Figure 4 and Table 3).

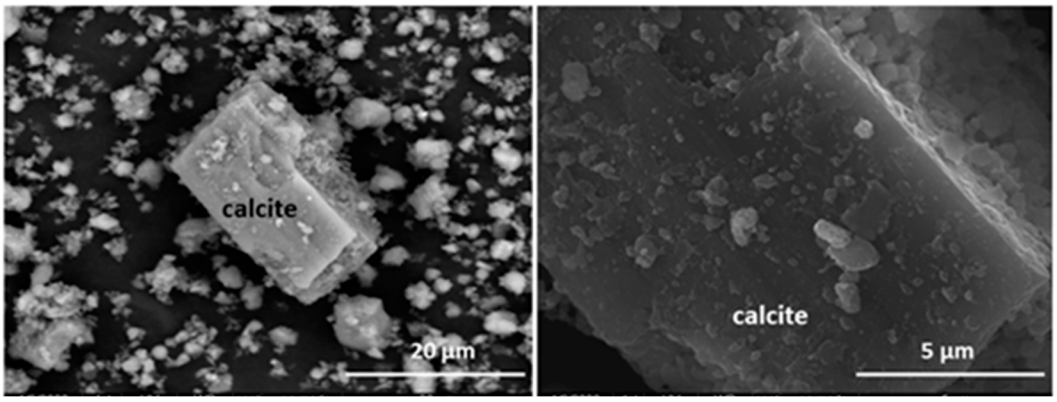

Figure 3. Microaggregates and surface deposits on rhombohedral calcite crystal (**left**). Detail of initial HcV waste surface (**right**).

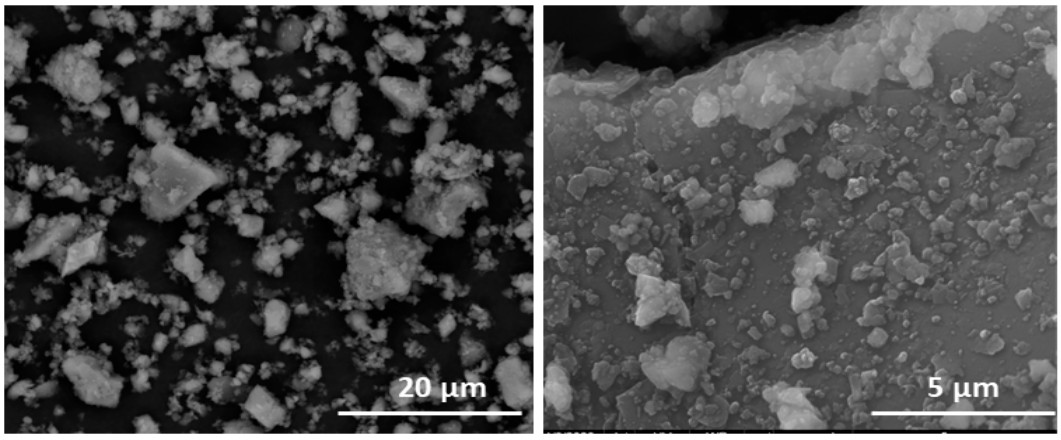

Figure 4. (**left**) Limestone aggregates in HcV. (**right**) Surface deposits on HcV.

Selective clustering by the elements comprising the siliceous and calcareous aggregates, along with variable material morphology, largely hindered the identification of these fragments with any of the minerals described (Figures 5 and 6; Tables 3 and 4). More sulphur was identified in the limestone than in the siliceous aggregates.

The siliceous aggregates exhibited low crystallinity that generated very open structures and scantly uniform, porous, uneven surfaces that favoured size reduction. All such anomalies induced an increase in the surface charge and for this reason; a higher surface reactivity is generated (Figure 5 and Table 4). In a saturated lime solution, such a reactive surface might serve as a substrate for pozzolanic reaction product growth.

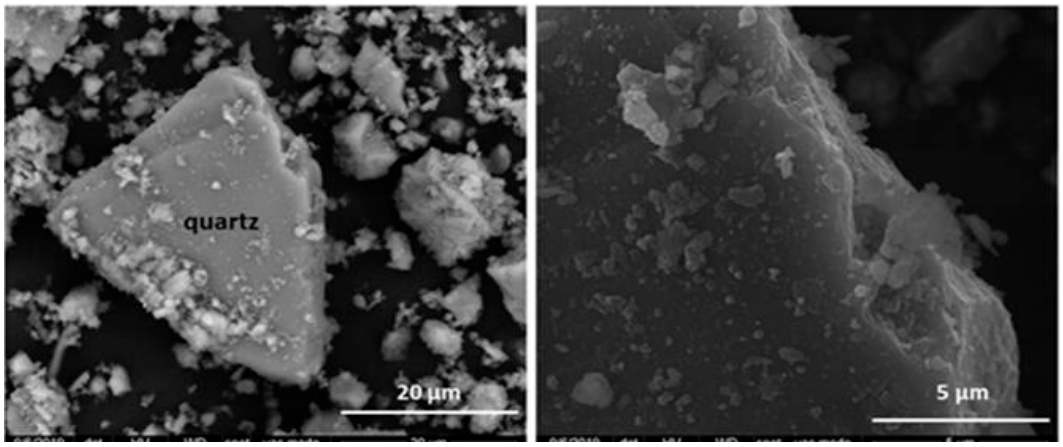

Figure 5. (**left**) Quartz and surface deposits. (**right**) Detail of deposits on initial HsC waste.

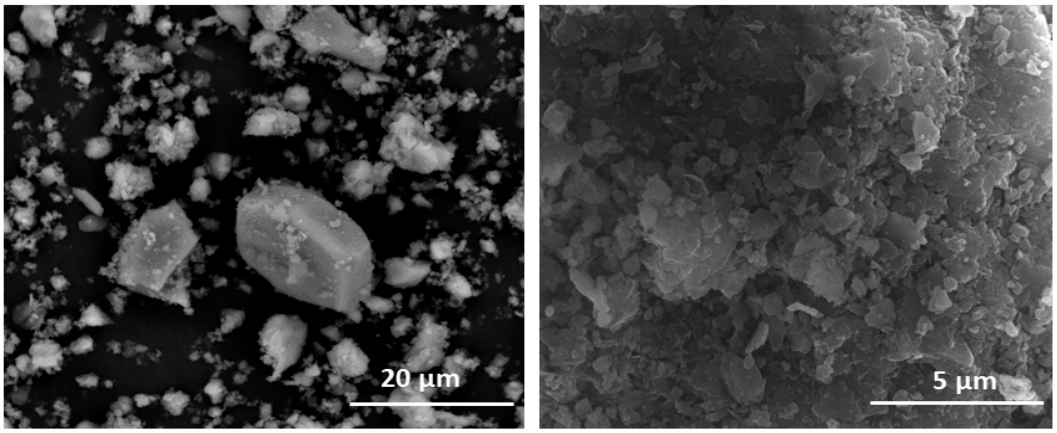

Figure 6. (**left**) Siliceous aggregates in HsT waste. (**right**) Detail of surface deposits on HsS waste.

Table 3. Energy dispersive X-ray spectroscopy **(**EDX) chemical analysis of limestone waste.

Oxide (%)	Ca Rich Aggregate	Fe Rich Aggregate	Calcite	Deposit on Calcite	Si rich Aggregate	S rich Aggregate
Al_2O_3	6.91 ± 2.18	1.82 ± 0.27	n.d.	3.88 ± 0.95	3.61 ± 1.25	6.59 ± 2.07
SiO_2	23.57 ± 4.16	2.85 ± 0.48	0.63 ± 0.11	9.79 ± 2.07	8.53 ± 3.26	14.31 ± 3.15
MgO	1.58 ± 0.59	7.96 ± 1.36	n.d.	0.64 ± 0.29	3.64 ± 0.58	1.05 ± 0.13
CaO	63.08 ± 4.32	3.56 ± 1.18	99.37 ± 2.59	83.93 ± 5.62	69.91 ± 5.46	50.79 ± 2.16
Fe_2O_3	1.66 ± 0.77	83.81 ± 4.29	n.d.	1.08 ± 0.33	5.48 ± 1.33	5.98 ± 2.31
SO_3	2.10 ± 1.07	n.d.	n.d.	n.d.	7.83 ± 3.52	19.76 ± 3.01
K_2O	0.80 ± 0.11	n.d.	n.d.	0.68 ± 0.18	0.93 ± 0.07	1.53 ± 0.42

n.d. = not detected.

Table 4. Energy dispersive X-ray spectroscopy **(**EDX) chemical analysis of siliceous waste.

Oxide (%)	Ti Rich Aggregate	Fe Rich Aggregate	Quartz	Deposit on Quartz	Si rich Aggregate
Al_2O_3	10.11 ± 2.37	13.36 ± 1.68	0.77 ± 0.21	7.82 ± 1.64	16.19 ± 2.25
SiO_2	39.27 ± 4.23	33.18 ± 2.94	98.81 ± 2.48	78.66 ± 3.82	51.94 ± 3.19
MgO	2.42 ± 0.99	2.60 ± 1.16	n.d.	1.04 ± 0.75	4.38 ± 1.24
CaO	33.43 ± 4.15	38.16 ± 3.21	0.41 ± 0.09	7.51 ± 2.47	16.08 ± 2.36
Fe_2O_3	1.11 ± 0.54	11.42 ± 2.25	n.d.	1.21 ± 0.83	2.22 ± 1.48
TiO_2	11.03 ± 1.03	0.76 ± 0.13	n.d.	n.d.	n.d.
Na_2O	1.09 ± 0.12	n.d.	n.d.	0.55 ± 0.21	2.72 ± 0.86
K_2O	1.54 ± 0.36	0.51 ± 0.09	n.d.	3.20 ± 1.26	3.32 ± 1.73
SO_3	n.d.	n.d.	n.d.	n.d.	3.15 ± 1.07

n.d. = not detected.

Wastes HsT and HcG were chosen as examples of the two waste types for ^{29}Si and ^{27}Al NMR microstructural analysis. The ^{29}Si spectrum for waste HcG reproduced in Figure 7 contains an intense narrow signal peaking at −72.3 ppm and a shoulder at −69 ppm. Both were generated by the Q^0 units present in anhydrous cement phases C_2S and C_3S. The wide Q^2 signal peaking at −86.4 ppm might be attributed to the presence of C–S–H gels or feldspars. Two small vibrations in the Q^3 zone might also be associated with the feldspars presence. A narrow signal at −107.3 ppm (Q^4) was generated by quartz and/or reactive silica [41–46].

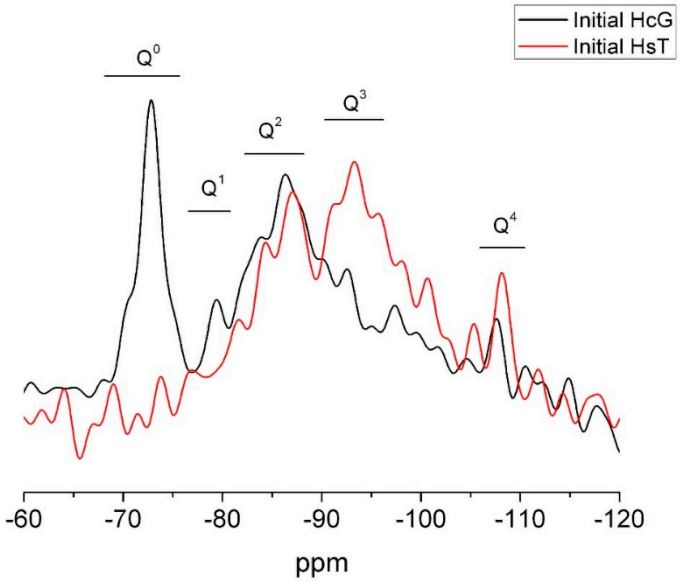

Figure 7. ^{29}Si NMR spectrum for initial wastes HsT and HcG.

The ^{29}Si NMR spectrum for siliceous waste HsT (Figure 7) had two wide bands characteristic of Q^2 and Q^3 units denoting the presence of silicates, perhaps in the form of C–S–H gels and/or feldspars, the latter at a higher percentage than in calcareous HcG. A signal for Q^4 units attributable to quartz and (reactive) amorphous silica was also observed, as expected. No Q^0 signals were detected in this sample, an indication of the absence of cement anhydrous phases, primarily C_2S and C_3S, corroborating the XRD and SEM/EDX findings.

The ^{27}Al NMR spectra for wastes HcG and HsT reproduced in Figure 8 exhibited tetrahedrally and octahedrally coordinated Al. Whilst the Al(VI) amount was similar in the two materials, much more tetrahedral Al was observed in siliceous waste HsT, in keeping with the higher percentage of Al_2O_3 detected in that sample in the XRF analysis.

The Al (IV) signals at approximately 55 ppm and 68 ppm may be attributed not only to the presence of tetrahedral aluminium in tecto- and phyllosilicate structures.

The infrared mid-range absorption bands for the calcareous waste are depicted in Figure 9 and for the siliceous materials in Figure 10. Although radiation was absorbed at the same vibration frequencies in all the spectra, relative intensities differed, further supporting the XRD findings.

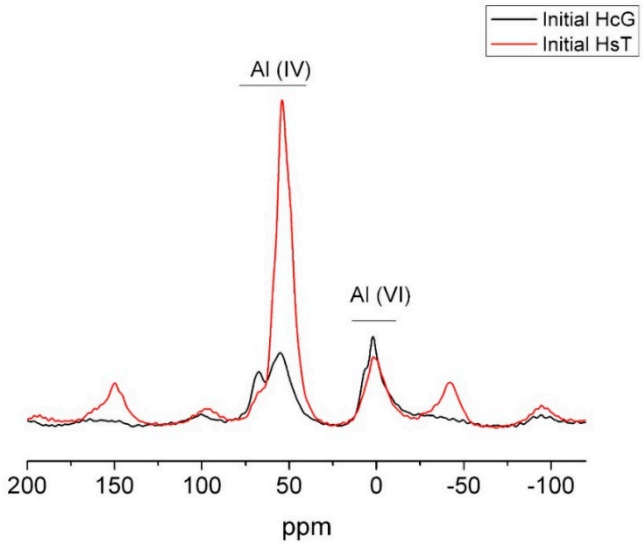

Figure 8. ^{27}Al NMR spectrum for initial wastes HsT and HcG.

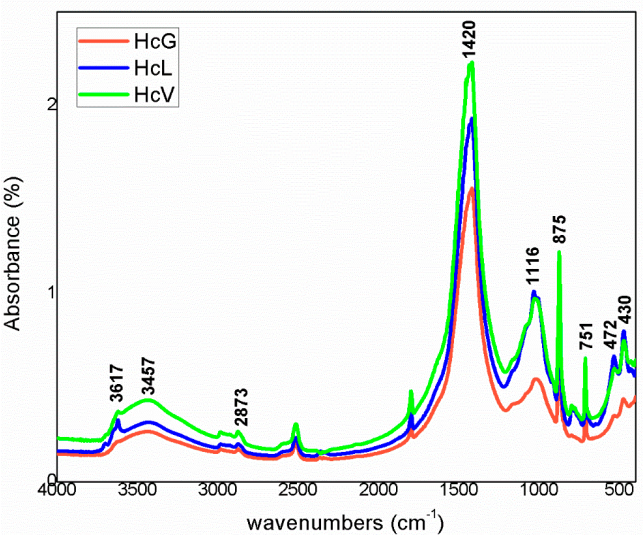

Figure 9. FTIR spectra for calcareous waste (Hc).

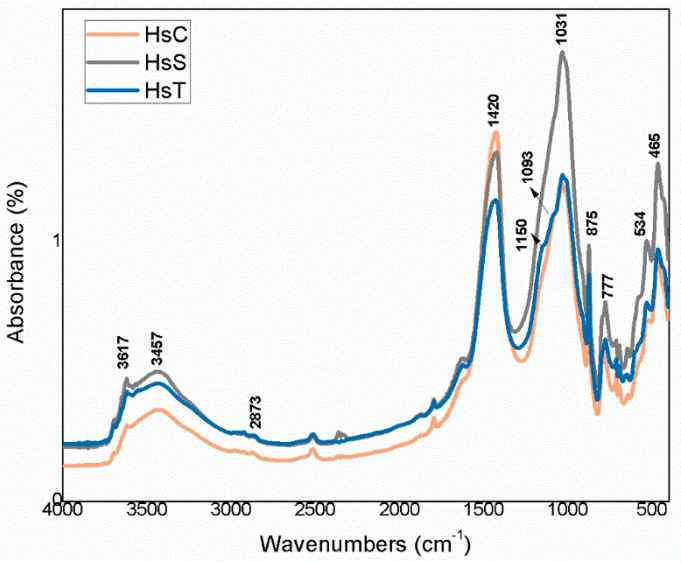

Figure 10. FTIR spectra for siliceous waste (Hs).

The bands were associated with vibrations generated by OH^- groups in the water on clay minerals and by CO_3^{2-} groups for calcite. The lower wavenumber bands, at 1200 cm^{-1} to 700 cm^{-1}, were attributed to the Si–O groups in quartz and phyllosilicates such as muscovite and kaolinite. In the lowest zone analysed, 600 cm^{-1} to 400 cm^{-1}, the vibrations were due to the Si–O–Al and Si–O–Si groups in those compounds.

The highest intensity signals on the spectra for calcareous waste (HcG-HcL-HcV), associated with calcium carbonate in the calcite form, generated bands with lower relative intensity on the spectra for siliceous waste (HsC-HsS-HsT). The bands peaking at 1087 cm^{-1}, 796 cm^{-1}, 777 cm^{-1} and 472 cm^{-1}, found on the spectra for all the fine particle waste but with particularly high relative intensity on those for the siliceous material, were attributed to quartz.

The bands peaking at 3695 cm^{-1}, 3675 cm^{-1}, 3652 cm^{-1}, 3617 cm^{-1} and 3457 cm^{-1} in the OH^- group vibration region (observed more clearly on the HcL spectrum than others), although assigned primarily to kaolinite, were also associated with mica, illite and muscovite. The lower intensity of the bands at 3675 cm^{-1} and 3652 cm^{-1} was indicative of low structural order, which would explain the failure of XRD to detect kaolinite in any of the samples except for a minor proportion in HcL.

3.2. Variation in Lime Fixed with Time

The variation in the percentage of lime fixed by the various types of fine particle CDW across the 90 days pozzolanic reaction is graphed in Figure 11. The three types of siliceous aggregate wastes exhibited similar behaviour; despite their origin from different recycle plants. The 90 days lime fixation value ranged from 60% to 67% and was highest for waste HsT.

The calcareous waste was observed to react less intensely with lime than the siliceous material, with some differences among the three samples. Whereas HcG reactivity remained practically unaffected by reaction time, with lime fixation values of around 20% across the entire period, the amount of lime fixed by HcL and HcV, grew with time to nearly 40% after 90 days.

Lime fixation, lower than observed in the pozzolanic materials traditionally used in commercial blended cement manufacture such as fly ash, silica fume and thermally activated pozzolans [47], was nonetheless similar to that reported for silico-manganese slag [48].

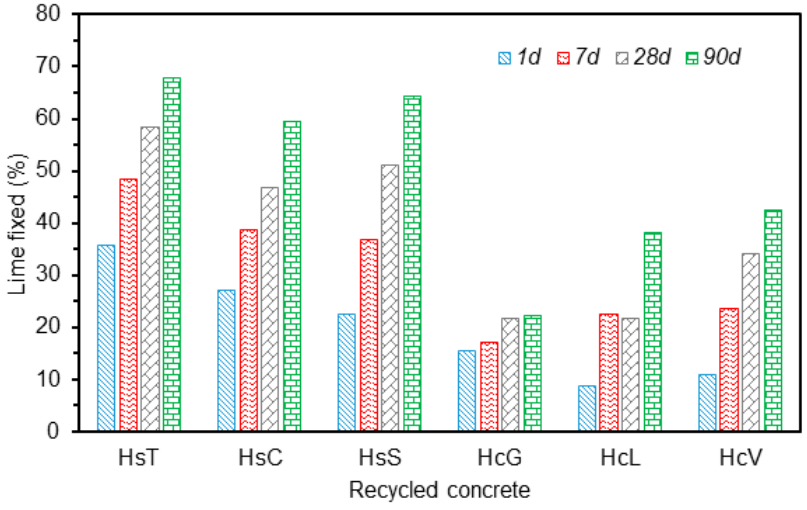

Figure 11. Variation in lime fixed with reaction time.

A kinetic-diffusive mathematical model was applied to determine pozzolanic reaction kinetics in the CDW/lime system. The variation in lime concentration over time in the samples analysed is compared in Figure 12.

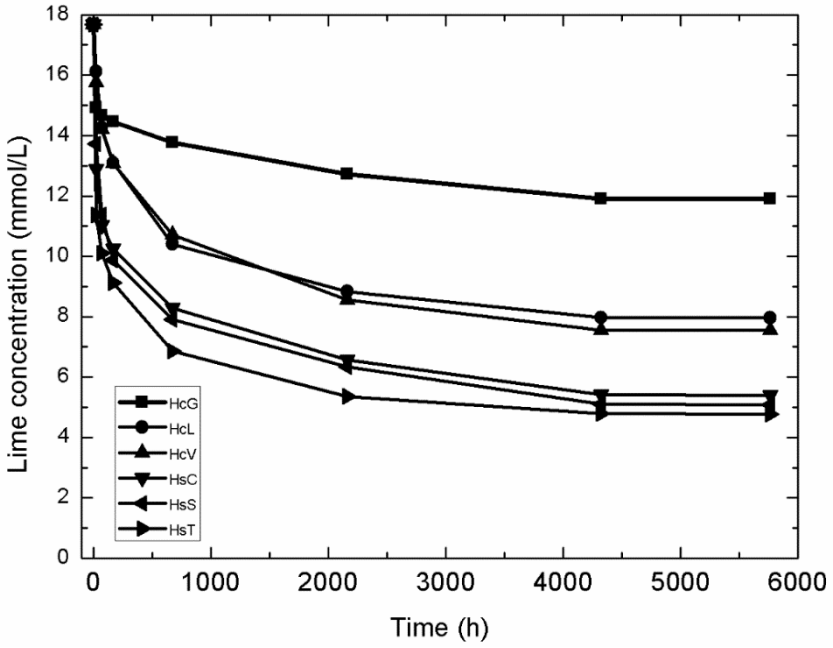

Figure 12. Variation in CDW lime concentration with time.

Pozzolanic reaction kinetics was calculated for the quantitative characterisation of CDW pozzolanicity. Using the method by kinetic-diffusive model expressed as shown below (Villar-Cociña et al. [49–52]) was used to describe the pozzolanic reaction in a pozzolan/CH solution system.

$$C_t = \frac{0.23\,.Exp\left(\frac{-3t}{\tau}\right).\left(-1+Exp\left(\frac{t}{\tau}\right)\right).\frac{1}{\tau}}{D_e\, r_s} + \frac{0.23.Exp\left(-\frac{t}{\tau}\right).\frac{1}{\tau}}{K\, r_s{}^2} + C_{corr} \quad (1)$$

where D_e is the effective diffusion coefficient; K the reaction rate constant; τ a constant denoting the time required for the radius of the pozzolanic particle to decline to 37% of its initial value (r_s), defined here as 0.090 mm; Ct the absolute decline in lime concentration over time in the pozzolan/lime system; and C_{corr} a term to correct for the residual CH not consumed in the reaction.

The kinetic parameters, the reaction rate constant in particular, were calculated by fitting the absolute decline in lime concentration to time with the aforementioned model. The τ and K values yielded by the model are given in Table 5, along with correlation coefficient r and determination coefficient R^2. Further to the K values, which provide a direct measure of a material's pozzolanicity, all the samples exhibited low pozzolanicity, on the order of 10^{-4} h^{-1}.

Table 5. Reaction rate constants K and τ, correction factor C_{corr}, correlation coefficient r and multiple determination coefficients R^2 for the fine particle CDWs studied.

Waste	τ (h)	Reaction Rate Constant (K·h^{-1})	C_{corr}	R	R^2
HcG	140.3 ± 15.2	(1.18 ± 0.12). 10^{-4}	12.52 ± 0.4	0.8765	0.8548
HcL	141.9 ± 16.1	(1.62 ± 0.91). 10^{-4}	8.91 ± 0.51	0.9364	0.9281
HcV	162.2 ± 18.4	(1.27 ± 0.95). 10^{-4}	8.69 ± 0.65	0.9340	0.9231
HsC	112.5 ± 10.6	(3.49 ± 0.82). 10^{-4}	6.54 ± 0.79	0.9067	0.8987
HsS	124.1 ± 12.2	(3.06 ± 0.94). 10^{-4}	6.15 ± 0.63	0.9225	0.9115
HsT	87.7 ± 8.4	(6.58 ± 0.98). 10^{-4}	5.68 ± 0.83	0.9006	0.8943

Although all six types of waste exhibited low pozzolanicity, reactivity was lowest and fairly uniform in calcareous wastes HcL, HcV and HcG. Siliceous wastes HsT, HsC and HsS were more reactive with similar values recorded for the latter two and the highest for HsT.

3.3. Variation in Mineralogical Phases during the Pozzolanic Reaction

The XRD patterns reproduced in Figure 13 for the HcL/lime system, taken by way of example of all the types of waste analysed, show the variations in the mineralogical and hydrated phases. The Rietveld quantification values for all six types of waste are listed in Table 6.

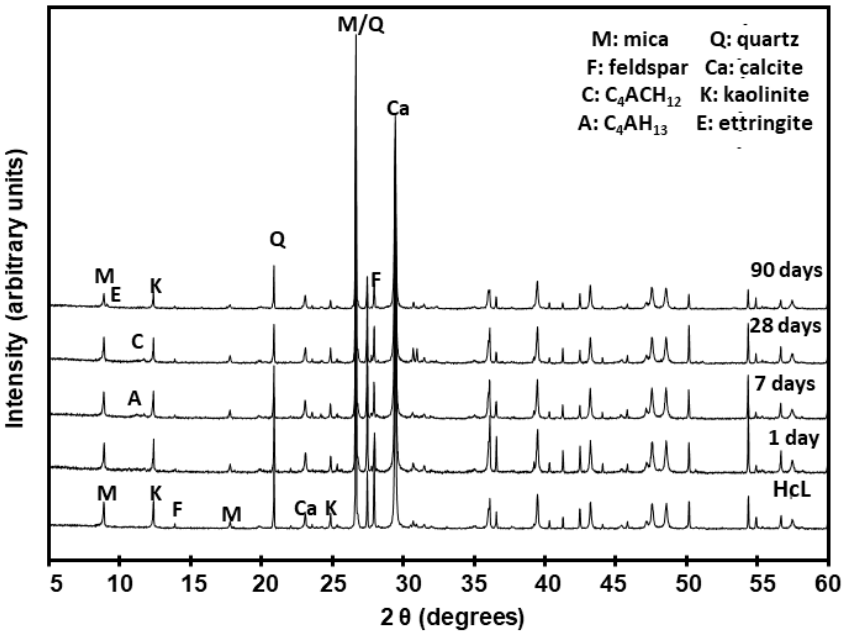

Figure 13. XRD patterns for initial waste HcL and after reaction with lime.

An analysis of the mineralogical findings confirmed that the new systems contained the initial minerals as well as neo-forming phases, more clearly identified with SEM/EDX, for the low concentrations involved in some cases hindered quantification of the XRD patterns.

The initial composition of the waste favoured the formation of new phases such as ettringite [53,54], calcium aluminate hydrates and C–S–H gels very early into the reaction with the saturated lime solution (SLS). C–S–H and C–S–A–H gels formed clusters of small wrinkled plates throughout the pozzolanic reaction. Ettringite adopted the form of fibres [55,56] and like the gels was observed at all reaction times, whereas the aluminate laminas appeared at 7 days or 28 days.

These hydrated products nucleated on the initial mineralogical phases, especially the highly alterable amorphous phases and feldspars. In that process, the highly flawed aggregate surfaces, with voids, fractures and randomly scattered materials of varied composition described as amorphous phases (Figure 14 and Table 7), favoured the nucleation of new materials.

Table 6. Rietveld refinement for six types of fine particle CDW (M: mica, Q: quartz; F: feldspar, C: calcite; Ett: ettringite; Am. Mat.: amorphous material; K: kaolinite; n.d.: not detected; t: traces; X^2: Rietveld goodness of fit; R_B: Bragg R factor).

Waste	Time (Days)	M (%)	Q (%)	F (%)	C (%)	C_4AH_{13} (%)	Ett (%)	Am. Mat. (%)	C_4ACH_{12} (%)	K (%)	R_B	X^2
HcG	initial	10	9	11	52	n.d.	n.d.	17	n.d.	n.d.	23.9	6.9
	1	10	9	11	52	n.d.	n.d.	18	n.d.	n.d.	21.6	67
	7	10	9	10	51	T	n.d.	20	n.d.	n.d.	22.5	7.2
	28	10	9	9	51	n.d.	n.d.	21	n.d.	n.d.	21.4	6.5
	90	10	9	9	47	n.d.	t	25	n.d.	n.d.	19.4	5.5
HcL	initial	12	14	13	40	n.d.	n.d.	11	n.d.	10	17.9	6.2
	1	12	14	10	42	n.d.	n.d.	12	n.d.	10	20.5	5.7
	7	10	14	8	45	1	n.d.	12	t	10	21.3	6.4
	28	8	14	8	48	T	n.d.	13	1	8	19.9	5.9
	90	6	14	6	51	n.d.	t	17	n.d.	6	18,7	6.9
HcV	Initial	7	12	10	62	n.d.	n.d.	9	n.d.	t	16.8	5.7
	1	7	12	10	63	n.d.	n.d.	8	n.d.	n.d.	18.2	6.3
	7	7	12	8	59	T	n.d.	14	n.d.	n.d.	15.5	5.7
	28	5	10	4	64	n.d.	t	17	n.d.	n.d.	17.3	6.1
	90	5	10	2	63	n.d.	t	20	n.d.	n.d.	19.2	7.4
HsC	initial	6	49	6	28	n.d.	n.d.	11	n.d.	n.d.	19.1	7.7
	1	4	49	4	31	n.d.	n.d.	12	n.d.	n.d.	17.5	5.9
	7	4	49	2	38	n.d.	n.d.	7	n.d.	n.d.	18.5	6.2
	28	2	49	6	35	n.d.	n.d.	8	n.d.	n.d.	15.9	5.4
	90	2	39	10	35	n.d.	t	4	n.d.	n.d.	16.1	6.1
HsS	initial	4	58	10	16	n.d.	n.d.	12	n.d.	n.d.	22.3	8.2
	1	4	58	8	18	n.d.	n.d.	11	n.d.	n.d.	32.4	9.3
	7	3	58	6	24	n.d.	n.d.	8	n.d.	n.d.	20.9	7.5
	28	3	58	4	28	n.d.	n.d.	6	n.d.	n.d.	16.3	5.2
	90	3	58	4	28	1	t	5	n.d.	n.d.	15.8	4.9
HsT	initial	4	48	8	24	n.d.	n.d.	16	n.d.	n.d.	17.6	7.3
	1	3	48	11	24	n.d.	n.d.	14	n.d.	n.d.	18.5	8.1
	7	2	48	10	28	n.d.	t	12	n.d.	n.d.	19.2	6.3
	28	2	48	8	31	n.d.	t	11	n.d.	n.d.	17.1	5.7
	90	2	48	8	31	n.d.	t	11	n.d.	n.d.	16.4	5.8

C–S–H and C–S–A–H gels are the first to nucleate on the aggregate surfaces; then are growth substrates for the laminar aluminates or ettringite. The random distribution of elements in the aggregates explains the uneven arrangement of the hydrated phases. Ettringite nucleated in the presence of sulphur [57–59], while the laminar $C4A\bar{H}11$ structures formed where calcite is major.

Table 7. EDX chemical analysis of 1 day HcG waste/lime system.

Oxide (%)	C–S–H Gel	Ettringite	$C_4A\bar{H}_{11}$
Al_2O_3	10.19 ± 0.52	27.70 ± 2.12	31.08 ± 1.27
SiO_2	17.31 ± 0.88	4.27 ± 0.95	3.21 ± 0.92
SO_3	n.d.	21.16 ± 0.72	8.99 ± 0.51
MgO	1.73 ± 0.26	n.d.	n.d.
CaO	70.77 ± 2.39	46.87 ± 2.28	56.72 ± 1.83

(n.d. = not detected).

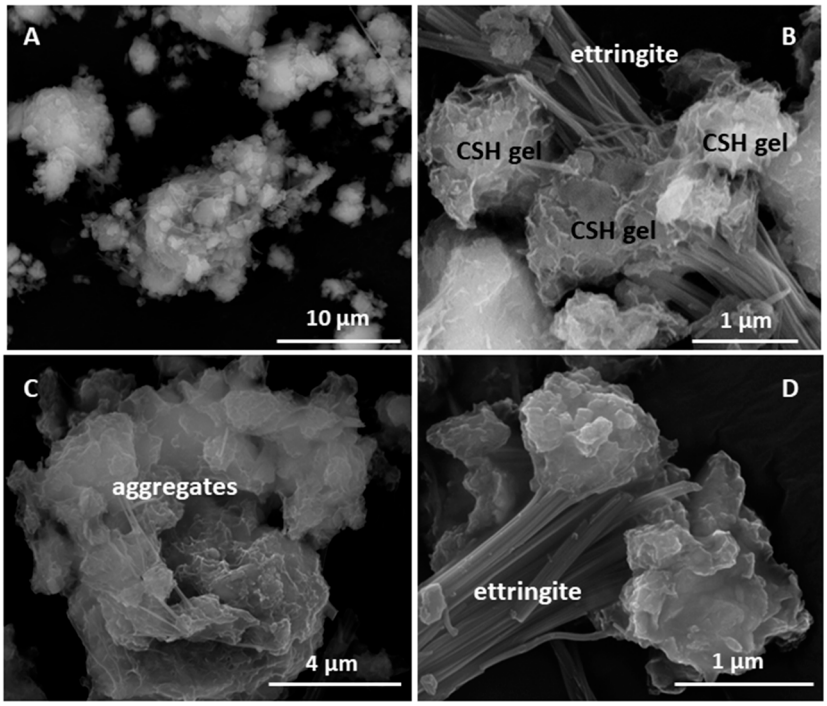

Figure 14. (**A**) Overview of HcG; (**B**) ettringite and C–S–H gel in HcG, detail; (**C**) overview of aggregates in HcC; (**D**) ettringite in HcC.

The signal for Q^2 units on the ^{29}Si NMR spectrum for HcG, which could include the Q^2 (1Al) units present in C–S–H gels, was more intense for the 90 days than the initial sample (Figure 15). In contrast, the signals for the Q^3 and Q^4 units disappeared on the 90 days spectrum. As quartz was inert in all the waste types at all ages, the absence of Q^4 signals on the 90 days NMR spectrum would indicate that they were generated by the reactive silica present in the amorphous phase, consumed during the pozzolanic reaction.

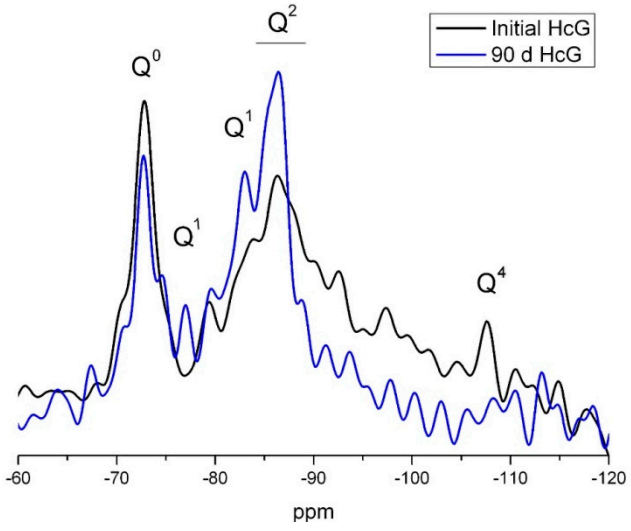

Figure 15. ^{29}Si NMR spectrum for 0 day and 90 days HcG waste.

The ^{27}Al NMR spectra for 1 day and 90 days calcareous waste HcG are depicted in Figure 16. The two new Al (VI) signals were also identified by SEM. The one at 13.4 ppm denoted ettringite formation, while the other, at 9.6 ppm, was generated by a calcium aluminate hydrate, very likely C_4AH_{13}. From Antoni et al. [60] should be considered also the possibility to carboaluminate hydrated phases formation with very close resonances, 10.30 ppm for hemicarboaluminate and 8.7

ppm for monocarboaluminate [61]. They formed at the expense of the anhydrous phases, the signals for which declined on the spectra.

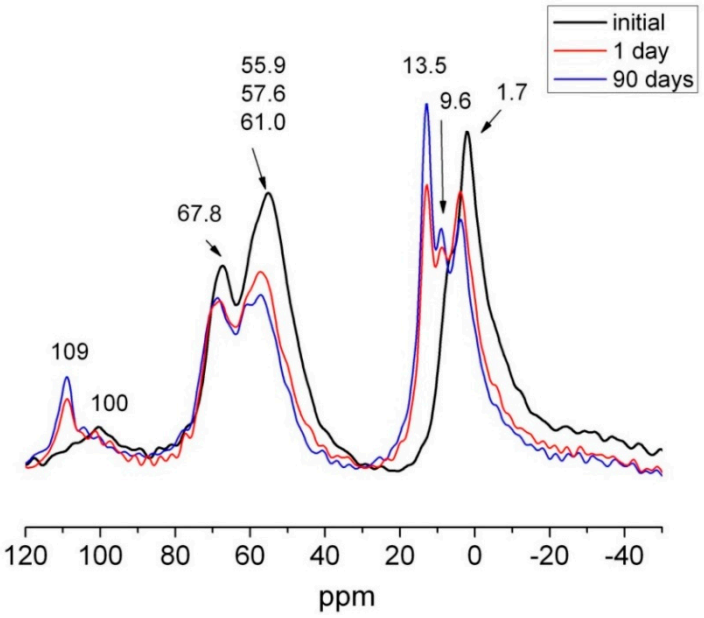

Figure 16. ^{27}Al NMR spectra for initial, 1 day and 90 days HcG.

Although the signals for the anhydrous phases also declined on the ^{27}Al NMR spectrum (Figure 17) for siliceous waste HsT, the spectrum denoted ettringite but no calcium aluminate hydrate formation, findings consistent with the SEM/EDX analysis.

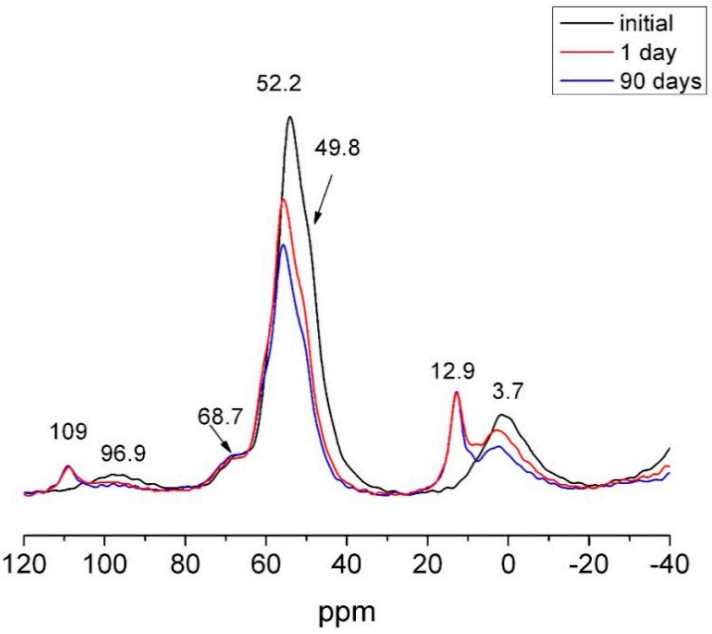

Figure 17. ^{27}Al NMR spectra for initial, 1 day and 90 days HsT.

The IR spectra for the 90 days samples in Figures 18 and 19 show the changes in the absorbance bands, whereas scantly any variation was visible on the spectra for the 1 day and 28 days samples. The most prominent changes included a decline in both some of the OH^- group bands in the 3700 cm^{-1} to 3400 cm^{-1} region and in the relative intensity, along with widening, of the 1100 cm^{-1} to 900 cm^{-1} Si–O stretching vibration bands. Those differences might be attributed to the

lower crystallinity, especially in Hs waste, of clay-like phases such as, kaolinite, muscovite, illite and mica.

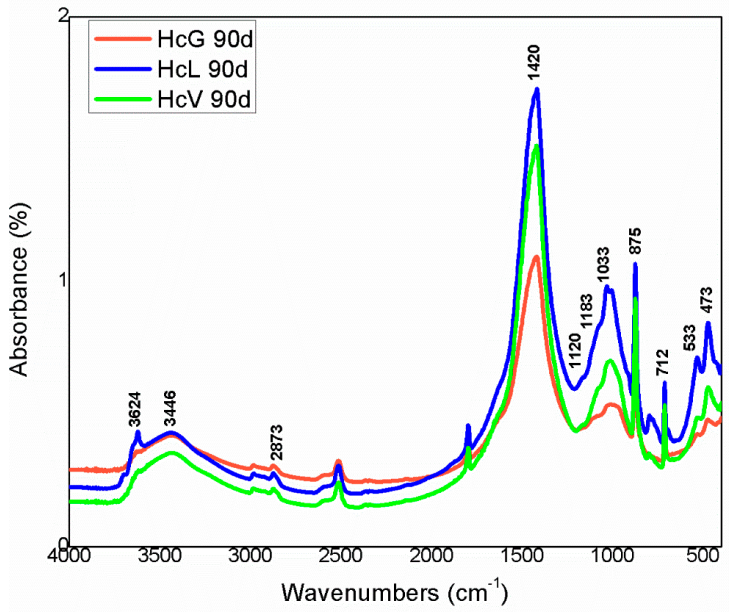

Figure 18. FTIR spectra for 90 days Hc waste.

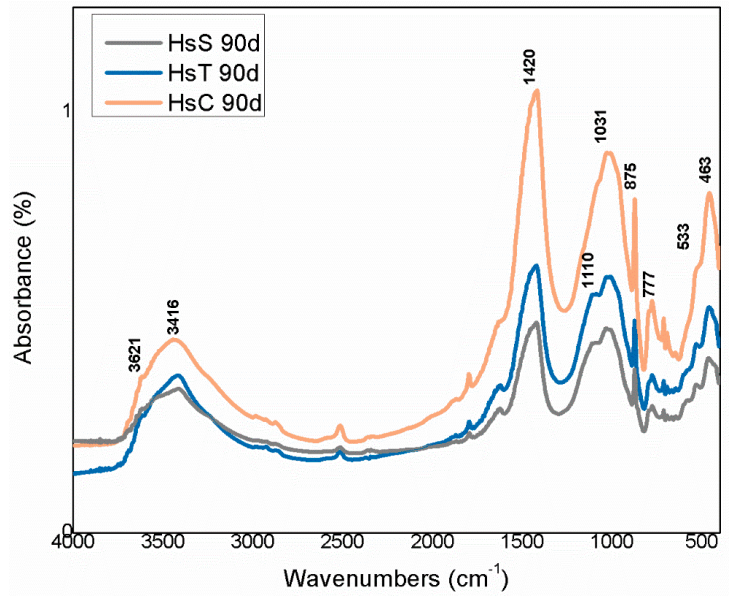

Figure 19. FTIR spectra for 90 days Hs waste.

4. Conclusions

The most prominent conclusions that can be drawn from the present findings are set out below.

Despite their differences in composition (recycled siliceous and calcareous aggregate) and origin (six waste management plants), the six types of fine particle (<5 mm) CDW analysed were mineralogically similar. Calcite, quartz, mica, feldspar and kaolinite, along with anhydrous cement phases, were detected in all six, although the concentrations varied depending on the type of recycled concrete aggregate involved. No C–S–H gels, ettringite, portlandite or other typical cement hydration products were identified, however.

Further to the lime fixation data gathered during the pozzolanic reaction and analysed with a kinetic-diffusion model, this fine concrete waste exhibited medium-low fixation capacity, which was nonetheless higher in the siliceous than in the calcareous materials.

Those pozzolanicity findings were corroborated by analyses conducted on the post-reaction solid residue. Although new mineralogical phases such as ettringite, aluminates (C_4AH_{13}, C_4AcH_{12}) and C–S–H gels were clearly identified, only small quantities of each were detected.

C–S–H gel and ettringite formed from the outset and throughout the pozzolanic reaction. The calcium aluminates (C_4AH_{13} and C_4ACH_{13}) were first identified at 7 days or 28 days. These phases nucleated on the starting materials, primarily the greatly altered amorphous components and feldspars.

In light of its characteristics as determined in this study, the fine particle (<5 mm to 6 mm) waste resulting from crushing concrete-based CDW at management plants reacts moderately with portlandite and may consequently be apt for reuse as an eco-pozzolan. Future research would be required to analyse that promising finding by assessing the performance of such new eco-efficient cement matrices.

Author Contributions: M.F. planned the experiments and drafted the manuscript. R.G.-G. and R.V.d.l.V. helped structure the write-up and conducted the XRD and SEM-EDX trials. S.M.-R. conducted the NMR and L.F.-C. the FTIR analyses. E.V.-C. performed the kinetic-diffusive model calculations. The manuscript was reviewed by all the authors, who approved the final draft.

Funding: This research was funded by Spain's Ministry of Science, Innovation and Universities under National Project RTI2018-097074-B-C21, the EU's ERDF, the Spanish National Research Agency (AEI), the Spanish Construction and Demolition Waste Recycling Association (RCDA), Sika (Madrid, Spain) and the Spanish Institute of Cement and its Applications (IECA).

Conflicts of Interest: The authors declare no conflicts of interest.

References

1. Hafliger, I.F.; John, V.; Passer, A.; Lasvaux, S.; Hoxha, E.; Saade, R.M.; Habert, G. Buildings environmental impacts' sensitivity related to LCA modelling choices of construction materials. *J. Clean. Prod.* **2017**, *156*, 805–816.
2. Oliveira, M.L.S.; Izquierdo, M.; Querol, X.; Lieberman, R.N.; Saikia, B.K.; Silva, L.F.O. Nanoparticles from construction wastes: A problem to health and the environment. *J. Clean. Prod.* **2019**, *219*, 236–243.
3. Chinda, T. Investigation of factors affecting a construction waste recycling decision. *Civ. Eng. Environ. Syst*. **2016**, *33*, 214–226.
4. EU Construction and Demolition Waste. Protocol and Guidelines. Available online: https://ec.europe.eu/growth/content/eu-construction and demolition protocol-0 (accessed on 12 January 2020).
5. Medina, C.; Zhu, W.; Howind, T.; Frías, M.; Sanchez de Rojas, M.I. Effect of the constituents (asphalt, clay materials, floating particles and fines) of construction and demolition waste on the properties of recycled concretes. *Constr. Build. Mater*. **2015**, *79*, 22–33.
6. Asociación Española de Residuos de Construcción y Demolición. *Informe Producción y Gestión de RCDs en España 2011–2015*; Asociación Española de Residuos de Construcción y Demolición: Madrid, Spain, 2017.
7. Khudyakova, L.I.; Kislov, E.V.; Paleev, P.L.; Kotova, I.Y. Nephrite-bearing mining waste as a promising mineral additive in the production of new cement types. *Minerals* **2020**, *10*, 394.
8. Moreno-Pérez, E.; Hernández-Ávila, J.; Rangel-Martínez, Y.; Cerecedo-Sáenz, E.; Arenas-Flores, A.; Reyes-Valderrama, M.I.; Salinas-Rodríguez, E. Chemical and mineralogical characterization of recycled aggregates from construction and demolition waste from Mexico City. *Minerals* **2018**, *8*, 237.
9. Circular Economy Action Plan. Available online: https://ec.europa.eu/environment/circular-economy/ (accessed on 15 January 2020).
10. *Guía Español de Áridos Reciclados Procedentes de RCD.*; Proyecto Gear; Government of Spain: Madrid, Spain, 2012.
11. Gastaldi, D.; Canonico, F.; Capelli, L.; Buzzi, L.; Boccaleri, E.; Irico, S. An investigation on the recycling of hydrated cement from concrete demolition waste. *Cem. Concr. Comp*. **2015**, *61*, 29–35.

12. Fernández Ledesma, E.; Fernaádez Rodríguez, J.M.; Jiménez, J.R.; Galvin, A.P. Properties of masonry mortars manufactured with fine recycled concrete aggregates. *Const. Buil. Mat.* **2014**, *71*, 289–298.
13. Florea, M.V.A.; Ning, Z.; Brouwers, H.J.H. Activation of liberated concrete fines and their application in mortars. *Const. Buil. Mat.* **2014**, *50*, 1–12.
14. Zou, G.; Zhang, J.; Liu, X.; Lin, Y.; Yu, H. Design and performance of emulsified asphalt mixtures containing construction and demolition waste. *Constr. Build. Mater*. **2020**, 239, doi:10.1016/j.conbuildmat.2019.117846.
15. Šljivić-Ivanović, M.; Smičiklas, I. Utilization of C&D waste in radioactive waste treatment—Current knowledge and perspectives. In *Advances in Construction and Demolition Waste Recycling*; Pacheco-Torgal, F., Ding, Y., Koutamanis, A., Eds.; Woodhead Publishing: Cambridge, UK, 2020; Chapter 23, pp. 475–500.
16. Asensio, E.; A.; Medina, C.; Frías, M.; Sánchez de Rojas, M.I. Clay-based construction and demolition waste as a pozzolanic addition in blended cements. Effect on sulfate resistance. *Constr. Build. Mater.* **2016**, *127*, 950–958.
17. Asensio, E.; Medina, C.; Frías, M.; Sánchez de Rojas, M.I. Characterization of Ceramic-Based Construction and Demolition Waste: Use as Pozzolan in Cements. *J. Am. Ceram. Soc.* **2016**, *99*, 4121–4127.
18. Asensio, E.; Medina, C.; Frías, M.; Sánchez de Rojas, M.I. Use of clay-based construction and demolition waste as additions in the design of new low and very low heat of hydration cements. *Mater. Struct.* **2018**, *51*, 101–111.
19. Medina, C.; Banfill, P.F.G.; Sánchez de Rojas, M.I.; Frías, M. Rheological and calorimetric behaviour of cements blended with containing ceramic sanitary ware and construction/demolition waste. *Constr. Build. Mater.* **2013**, *40*, 822–831.
20. Krour, H.; Trauchessec, R.; Lecomte, A.; Diliberto, C.; Barnes-Davin, L.; Bolze, B.; Delhay, A. Incorporation rate of recycled aggregates in cement raw meals. *Constr. Build. Mater.* **2020**, *248*, doi:10.1016/j.conbuildmat.2020.118217.
21. Contreras, M.; Teixeira, S.R.; Lucas, M.C.; Lima, L.C.N.; Cardoso, D.S.L.; da Silva, G.A.C.; Gregório, G.C.; de Souza, A.E.; dos Santos, A. Recycling of construction and demolition waste for producing new construction material (Brazil case-study). *Constr. Build. Mater.* **2016**, *123*, 594–600.
22. Omrane, M.; Rabehi, M. Effect of natural pozzolan and recycled concrete aggregates on thermal and physico-mechanical characteristics of self-compacting concrete. *Constr. Build. Mater*. **2020**, *247*, doi:10.1016/j.conbuildmat.2020.118576.
23. Ferreira, S.R.L.; Anjos, M.A.S.; Nóbrega, A.K.C.; Pereira, J.E.S.; Ledesma, E.F. The role of powder content of the recycled aggregates of CDW in the behaviour of rendering mortars. *Constr. Build. Mater.* **2019**, *208*, 601–612.
24. Jesus, S.; Maia, C.; Brazão, C.; de Brito, J.; Veiga, R. Rendering mortars with incorporation of very fine aggregates from construction and demolition waste. *Constr. Build. Mater.* **2019**, *229*, 116844.
25. Ulsen, C.; Kahn, H.; Hawlitschek, G.; Masini, E.H.; Angulo, S.C.; John, V.M. Production of recycled sand from construction and demolition waste. *Constr. Build. Mater.* **2013**, *40*, 1168–1173.
26. European Commission. Resource Efficient Use of Mixed Wastes Improving Management of Construction and Demolition Waste. Final Report October 2017. Available online: https://op.europa.eu/en/publication-detail/-/publication/78e42e6c-d8a6-11e7-a506-01aa75ed71a1/language-en/format-PDF/source-118503004 (accessed on 10 October 2019).
27. *ACI 130R-19: Report on the Role of Materials in Sustainable Concrete Construction*; American Concrete Institute: Farmington Hills, MI, USA, 2019.
28. *Instrucción Española del Hormigón Estructural (EHE-08)*, 5th ed.; Ministerio de Fomento: Madrid, Spain, 2011.
29. *NBN B 15-001/ PTV 406. Standaardisatie Vangeprefabriceerde Voorgespannen Betonliggers voor Kunstwerken*; FEBEFAST: Belgium, Brussels, 2017.
30. *Standard DIN 4226-101. Recycled Aggregates for Concrete in Accordance with DIN EN 12620—Part 101: Types and Regulated Dangerous Substances*; German Institute for Standardization: Berlin, Germany, 2017.
31. *Standard NTC2008. Norme Tecniche per le Costruzioni*, Ministry of Infrastructure and Transport: Rome, Italy, 2008.
32. *Standard BS 8500-2:2015 Concrete—Complementary British Standard to BS EN 206. Specification for Constituent Materials and Concrete (+A2:2019)*; British Standards Institution: London, UK, 2015.

33. Moreno-Juez, J.; Vegas, I.; Gebremariam, A.T.; García-Cortés, V.; Di Maio, F. Treatment of end-of-life concrete in an innovative heating-air classification system for circular cement-based products. *J. Clean. Prod.* **2020**, doi:10.1016/j.jclepro.2020.121515.
34. Moore, M.; Reynolds, R.C. *X-ray Diffraction and the Identification and Analysis of Clay Minerals*, 2nd ed.; Oxford University Press: Oxford, UK, 1997.
35. Rietveld, H.M. A profile refinement method for nuclear and magnetic structures, *J. Appl. Crystal*. **1969**, *2*, 65–71.
36. Le Saoût, G.; Kocaba, V.; Scrivener, K.L. Application of the Rietveld method to the analysis of anhydrous cements. *Cem. Conc. Res.* **2011**, *41*, 133–148.
37. Putz, H.; Brandenburg, K. Phase Identification from Powder Diffraction, Crystal Impact. 1997. Available online: http://www.crystalimpact.com/match (accessed on 15 June 2019).
38. Tsubota, M.; Kitagawa, J. A necessary criterion for obtaining accurate lattice parameters by Rietveld method. *Sci. Reports* **2017**, *7*, 15381.
39. Gebauer, J.G.; Harnit, A.B. Microstructure and composition of the hydrated cement paste of an 84 old years old concrete bridge construction. *Cem. Concr. Res.* **1975**, *5*, 163–170.
40. Gao, X.; Yu, Q.L.; Brouwers, H.J.H. Apply ^{29}Si, ^{27}Al MAS NMR and selective dissolution in identifying the reaction degree of alkali activated slag-fly ash composites. *Ceram. Inter.* **2017**, *43*, 12408–12419.
41. Hansen, M.R.; Jakobsen, H.J.; Sbisted, J. ^{29}Si chemical shift anisotropies in calcium silicates from high-field ^{29}Si MAS NMR spectroscopy. *Inorg. Chem.* **2003**, *42*, 2368–2377.
42. Spearing, D.R.; Stebbins, J.F. The ^{29}Si shielding tensor in low quartz. *Am. Mineral.* **1989**, *74*, 956–959.
43. Skibsted, J.; Henderson, E.; Jakobsen, H.J. Characterisation of calcium aluminate phases in cements by ^{27}Al MAS NMR spectroscopy. *Inor. Chem.* **2003**, *32*, 1013–1027.
44. Müller, D.; Gessner, W.; Samoson, A.; Lippmaa, E.; Scheler, G. Solid-state ^{27}Al NMR studies on polycrystalline aluminates of the system CaO-Al_2O_3. *Polyhedron* **1986**, *5*, 779–785.
45. Faucon, P.; Charpentier, T.; Bertrandie, D.; Nonat,A.; Virlet, J.; Petit, J.C. Characterisation of calcium aluminate hydrates and related hydrates of cement pastes by ^{27}Al MQ-MAS NMR. *Inorg. Chem.* **1998**, *37*, 3726–3733.
46. Plevova, E.; Vaculikova, L.; Valovicova, V. Thermal analysis and FT-IR spectroscopy of synthetic clay mineral mixtures. *J. Therm. Anal. Calorim*. **2020**, doi:10.1007/s10973-020-09527-9.
47. Sánchez de Rojas, M.I.; Frías, M. The pozzolanic activity of different materials. Its influence on the hydration heat in mortars, *Cem. Concr. Res*. **1996**, *26*, 203–2213.
48. Frías, M.; Sánchez de Rojas, M.I.; Cristina, C. The influence of SiMn slag on chemical resistance of blended cement pastes. *Constr. Build. Mater*. **2009**, *23*, 1472–1475.
49. Villar-Cociña, E.; Valencia, E.; González-Rodriguez, R.; Hernández-Ruiz, J. Kinetics of the pozzolanic reaction between lime and sugar cane straw ash by electrical conductivity measurement: A kinetic-diffusive model. *Cem. Concr. Res.* **2003**, *33*, 517–524.
50. Villar-Cociña, E.; Frías, M.; Valencia, E.; Sánchez de Rojas, M.I. An evaluation of different kinetic models for determining the kinetic coefficients in sugar cane straw-clay ash/lime system. *Adv. Cem. Res.* **2006**, *18*, 17–26.
51. Frías, M.; Villar-Cociña, E.; Sánchez de Rojas, M.I.; Valencia-Morales, E. The effect of different pozzolanic activity methods on the kinetics constants of the pozzolanic reaction: Application of a kinetic-diffusive model. *Cem. Concr. Res.* **2005**, *35*, 2137–2142.
52. Villar-Cociña, E.; Frías, M.; Valencia-Morales, E. Sugar cane wastes as pozzolanic materials: Application of mathematical model. *ACI Mater. J.* **2008**, *105*, 258–264.
53. Qoku, E.; Bier, T.A.; Westphal, T. Phase in assemblage in ettringite-forming cement pastes: A X-Ray diffraction and thermal analyses characterization. *J. Build. Eng.* **2017**, *12*, 37–50.
54. Yu, J.; Qian, J.; Tang, J.; Ji, Z.; Fan, Y. Effect of ettringite seed crystals on the properties sulphoaluminate cement. *Constr. Build. Mater.* **2019**, *207*, 249–257.
55. Cody, A.M.; Lee, H.; Cody, R.D.; Spry, P.G. The effects of chemical environment on the nucleation, growth, and stability of ettringite ($Ca_3Al(OH)_6$) $(SO_4)_3 \cdot 26H_2O$. *Cem. Concr. Res.* **2004**, *34*, 869–881.
56. Shimada, Y.; Young, J.F. Thermal stability of ettringite in alkaline solutions at 80 °C. *Cem. Concr. Res.* **2004**, *34*, 2261–2268.
57. Glasser, F.P. The role of sulfate mineralogy and cure temperature in delayed ettringite formation. *Cem. Concr. Comp*. **1996**, *18*, 187–193.

58. Diamond, S. Delayed Ettringite Formation—Processes and Problems. *Cem. Concr. Comp.* **1996**, *18*, 205–215.
59. Escadeillas, G.; Aubert, J.E.; Segerer, M.; Prince, W. Some factors affecting delayed ettringite formation in heat-cured mortars. *Cem. Concr. Res.* **2007**, *37*, 1445–1452.
60. Antoni, M.; Rossen, J.; Martirena, F.; Scrivener, K. Cement substitution by a combination of metakaolin and limestone. *Cem. Concr. Res.* **2012**, *42*, 1579–1589.
61. Scrivener, K.; Snellings, R.; Lothenbach, B. *A practical Guide to Microstructural Analysis of Cementitious Materials*, 1st ed.; CCR Press, Boca Raton, FL, USA, 2016.